The Role of Shear and Tensile Failure in Dynamically Triggered Landslides

T. Gipprich,[1] R. Snieder,[1] R. Jibson,[2] and W. Kimman[1]

Abstract. The dynamic stress generated by earthquakes is one of the causes for triggering landslides. Many methods characterize the triggering of landslides, but the role of dynamic effects which produce slope instability is not fully understood. Current methods, such as pseudostatic analysis and Newmark's method, focus on earthquake accelerations to monitor landslide potential. These methods depend on shear failure to analyze instability, while the role of tensile failure is not clear. We develop a limit-equilibrium model to investigate the dynamic stress generated by a given ground motion due to a plane wave and use this to assess the role of shear and tensile failure in the initiation of slope instability. We do so by incorporating the modified Griffith failure envelope, which has the feature of combining shear and tensile failure in a single criterion, while the Mohr-Coulomb theory accounts for shear failure only. Tests of dynamic stress in both homogeneous and layered slopes demonstrate that two modes of failure exist, tensile failure in the upper meters of a slope and shear failure at greater depth. We derive equations that express the dynamic stress in the near-surface by the acceleration measured at the surface. These equations are used to approximately define the depth for each mechanism of failure. We find that, because of the depth at which they occur, shear and tensile failure may collaborate in slope failure.

1. Summary

Current methods used to model earthquake-triggered landslides include pseudostatic analysis and Newmark's method. Pseudostatic analysis is a limit-equilibrium analysis where the acceleration due to an earthquake is computed as an additional static body force acting on the slope. A factor of safety (FS) analysis is carried out for different acceleration values to determine which critical value brings the slope to failure, reducing the factor of safety below 1.0 [*Jibson*, 1993]. The factor of safety gives the stability of a slope as the ratio of resisting to driving forces. When this ratio is above 1.0, the slope is safe. When less than 1.0, the slope begins to move [*Jibson et al.*, 2000].

Newmark's method goes further by estimating the permanent slope displacement caused by an earthquake [*Newmark*, 1965]. The critical acceleration a slope can withstand during an earthquake is given by [*Jibson et al.*, 2000]

$$a_c = (FS - 1)g\sin(\alpha) \ , \tag{1}$$

where g is gravitational acceleration and α can be estimated as the slope angle. An acceleration larger than this value initiates sliding on a slope. Newmark's method is used to calculate the permanent displacement of the slope by integrating an earthquake acceleration-time history twice over the times that exceed the critical acceleration [*Jibson*, 1993; *Jibson et al.*, 2000].

While pseudostatic analysis and Newmark's method focus on earthquake accelerations to account for shear failure, we focus on dynamic stress generated from a given ground motion and how this causes both shear and tensile failure at the initiation of slope instability. Post-failure deformation of a slope is not analyzed in this limit-equilibrium method.

First, we describe the static and dynamic stress in a dry, infinite slope and the failure criterion used to define failure. By testing several wave propagation scenarios, we show that two modes of failure develop in homogeneous and layered slopes. This analysis shows that tensile failure, due to dynamic stress, occurs in the upper meters of a slope, while shear failure takes place at greater depth.

To further understand the regions of shear and tensile failure in a slope, we derive dynamic stress equations that relate dynamic stress in the near-surface to the acceleration at the surface. By specifying the peak ground acceleration (PGA) in this analysis, these equations produce dynamic stress as a function of depth and help to define the depth of each mechanism of failure.

With two distinct depths for shear and tensile failure, we show that the two failure mechanisms collaborate to cause slope failure. Since this project focuses on a limit-equilibrium method, we cannot model displacement of a slope, but can speculate about the role of shear and tensile failure in the deformation process.

2. Static Stress In A Slope

We first consider the static stress in a 2D unsaturated slope. We employ a simple static stress model for near-surface stress caused by gravity [*Savage and Swolfs*, 1992]. The coordinate system used throughout the project defines the x-direction parallel to the surface of the slope and depth, z, normal to the surface. In this work, the horizontal direction means parallel to the slope while vertical refers to the direction normal to the slope.

In our model, the near-surface is assumed to be linearly elastic and the infinite, planar slope is laterally constrained so material cannot expand in the direction parallel to the slope [*Mello and Pratson*, 1999]. Because of translational invariance of an infinite slope, stress does not depend on the horizontal location.

[1]Center for Wave Phenomena and Department of Geophysics, Colorado School of Mines, Golden, Colorado, USA.

[2]The United States Geological Survey, Golden, Colorado, USA.

Copyright 2005 by the American Geophysical Union.
0148-0227/05/$9.00

The governing equations of stress for this model are [*Jaeger and Cook*, 1976; *Savage and Swolfs*, 1992]

$$\sigma_{xx}^{static} = \frac{\lambda}{\lambda + 2\mu} \rho g z \cos(\theta) \ , \tag{2a}$$

$$\sigma_{zz}^{static} = \rho g z \cos(\theta) \ , \tag{2b}$$

$$\sigma_{xz}^{static} = \rho g z \sin(\theta) \ , \tag{2c}$$

where λ and μ are Lamé elastic constants, ρ is the density, g the gravitational acceleration, and θ the slope angle. The stress is defined to be positive for compressive, normal stress, and negative for tensile stress.

Before modeling the plane wave propagation through a slope, we carry out a static slope-stability analysis to find whether the slope is initially statically stable [*Jibson*, 1993]. We do so by increasing the slope angle to see at which point the slope fails. In this way, we can define a slope that is stable for the static stress, but that can fail dynamically.

When analyzing a static slope, a discrepancy becomes apparent between the static stress model given by the expressions (2a)-(2c), and other traditional models. Normally, to study the limit-equilibrium of a slope, a factor-of-safety analysis is completed on a static model which produces failure when the FS is 1.0 or below. The FS equation for a dry, cohesionless slope reduces to,

$$FS = \frac{\tan(\phi)}{\tan(\theta)} \ , \tag{3}$$

where ϕ is the internal angle of friction. Slope instability occurs when ϕ is equal to the slope angle, θ, or when $FS = 1.0$. We find that the static stress state (2a)-(2c), fails at a critical angle, θ, that is smaller than ϕ.

The assumption of a laterally constrained, infinite slope, that defines the stress (2a)-(2c), could be the reason that the critical angle differs from the internal angle of friction. In this model, the horizontal derivatives vanish, so material cannot expand laterally. Nevertheless, the assumptions of this stress model are widely used in soil mechanics, and we work with these equations to understand how dynamic stress leads to slope failure.

2.1. Dynamic Stress for a Plane Wave Incident on a Slope

We compute the dynamic stress created from a plane wave incident on a slope using a 1D finite element wave equation code. This incorporates second-order equations of motion that solve for displacement, u_x and u_z [*Haney*, 2004]. Since we are interested in tensile failure, we limit ourselves to analyzing P-SV waves.

Solutions of the form $F = (t - px, z)$ describe a plane wave moving in the x-direction in time with a horizontal slowness, p. In a medium varying with depth only, p is constant and known as the ray parameter of the incoming wave, that is given by [*Aki and Richards*, 2002]

$$p = \frac{\sin(i_p)}{v_p} = \frac{\sin(i_s)}{v_s} \ , \tag{4}$$

where i_p and i_s are the incidence angles that P- and S-waves make with the normal axis of the slope, and v_p and v_s are the P- and S-wave velocities, respectively. For this solution the x-derivative is related to the time derivative by

$$\frac{\partial F(t - px, z)}{\partial x} = -p \frac{\partial F(t - px, z)}{\partial t} \ . \tag{5}$$

The code produces displacement, velocity and acceleration as well as the stress components, $\sigma_{xx}^{dynamic}$, $\sigma_{zz}^{dynamic}$ and $\sigma_{xz}^{dynamic}$ for a given incoming wave. At the free surface, the boundary conditions state that the tractions vanish [*Aki and Richards*, 2002]:

$$\sigma_{zz}^{dynamic}(z = 0) = \sigma_{xz}^{dynamic}(z = 0) = 0 \ . \tag{6}$$

Once the dynamic stress is known, the total stress state is given by the sum of the dynamic and static components of stress:

$$\sigma_{ij}^{total} = \sigma_{ij}^{static} + \sigma_{ij}^{dynamic} \ . \tag{7}$$

In this model, we scale the acceleration produced for an incoming wave to a desirable PGA. Normally this acceleration is chosen as a value typical of earthquakes, between 0.1 and 1.0 g [*Jibson*, 1993]. We calculate the sum of the squares of the maximum horizontal a_x, and vertical a_z, acceleration values at the surface of the slope, and normalize it to the PGA. The normalization value is then multiplied with the dynamic stress components produced by the finite-element code.

Failure depends on the PGA of the incoming wave, and for each slope, there exists a PGA that initiates failure at one location for a given instant in time. As the PGA increases, the slope is in a state of post failure. The linear model that we use does not account for post-failure behavior. We therefore use the modest value of 0.1 g for the PGA,

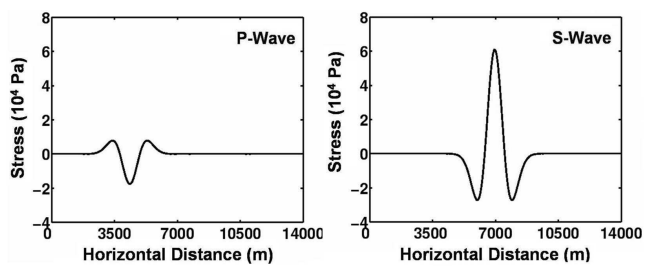

Figure 1. $\sigma_{xx}^{dynamic}$ component of stress for both 30° incident P- and S-waves at the surface of a slope for a PGA of 0.1 g. The S-wave produces larger stress at the surface than the P-wave.

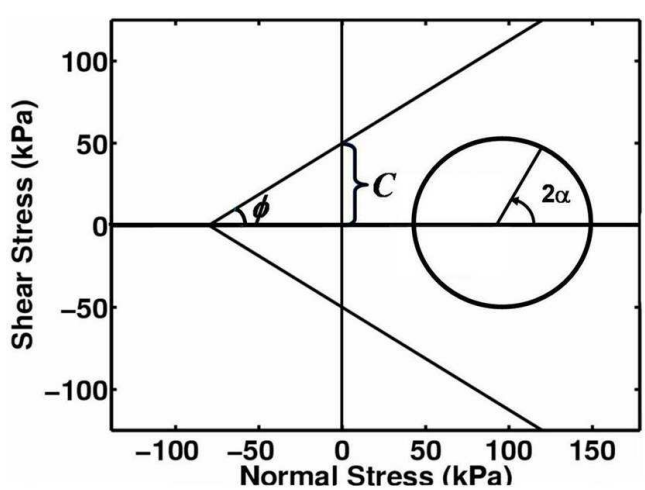

Figure 2. The Mohr circle and Mohr-Coulomb failure envelope. C is the cohesion of the slope and ϕ is the internal angle of friction. When failure occurs, α refers to the angle between the normal to the failure plane and the principal stress direction corresponding to σ_1.

and disregard the stress state in parts of the slope that are beyond failure. Proper design of earthquake-resistant structures require estimation of ground shaking in the 0.2-10 Hz frequency band [*Frankel*, 1999]. We use an incoming wave with a moderate peak frequency of 1.0 Hz.

We analyze both P- and S-waves in this project. When each is normalized to the same PGA, the S-wave produces larger dynamic stress at the surface of the slope than does the P-wave. Figure 1 shows a comparison of stress for P- and S-waves with an angle of incidence of 30°. This shows that after both waves are calibrated to a PGA of 0.1 g, the $\sigma_{xx}^{dynamic}$ component of stress at the surface is greater for the S-wave than for the P-wave.

We find for a variety of slope angles, that for both P- and S-waves, shear and tensile failure may occur in a slope. As a representative example, we show the dynamic stress generated by a 30° incident wave. Note that a normally incident wave only produces shear failure.

3. Determining Failure

Once a wave passes through a slope, dynamic stress is generated that may cause certain locations within the slope to fail. To understand the potential for failure, we address the behavior of the slope sediments under stress. For shear failure, this is commonly completed using a Mohr-Coulomb failure analysis. The Mohr circle, represented by principal stresses, is the basis for the Mohr-Coulomb failure analysis which tests whether stress exceeds strength. The shear strength of a failure surface in dry conditions is characterized by the Mohr-Coulomb failure criterion [e.g., *Bourne and Willemse*, 2001],

$$\tau = c + \sigma \tan(\phi) \ . \tag{8}$$

The angle ϕ is referred to as the internal angle of friction, which for sands is normally about 30°-34° [*Das*, 1997; *Selby*, 1993]. Cohesion strengthens a material and typically exists in soils containing clay. The values of cohesion for sands used in this analysis are smaller than those for solid rock, and range from 0-20 kPa [*Middleton and Wilcock*, 1994; *Selby*, 1993].

Figure 2 displays the Mohr circle and Mohr-Coulomb failure envelope. The Mohr circle produced at each location can change size due to the difference of static and dynamic stress through the slope. A post-failure state of stress represented by a Mohr circle lying outside of the envelope is not accounted for by our dynamic model. Failure takes place at a critical angle, $\alpha = (90° + \phi)/2$ [*Das*, 1997].

While the Mohr-Coulomb failure criterion is a common description of how materials fail, it can only be used to describe shear failure [*Bourne and Willemse*, 2001]. To determine the locations of both shear and tensile failure, we use another failure criterion that accounts for extensional stress and tensional failure.

The hypothesis produced by Griffith in 1921 states that as stress increases near the tips of thin, elliptical cracks, tensile failure eventually occurs. The tensile strength of a slope follows the parabolic Griffith criterion [*Bourne and Willemse*, 2001],

$$\tau^2 = 2c\sigma + c^2 \ . \tag{9}$$

A modification of this criterion, called the Modified Griffith Theory, has been introduced by *Brace* [1960] for combining tensile and shear failure into a single envelope (Figure 3). For small shear stress, the curved part of the envelope is defined by the Griffith equation, describing tensile

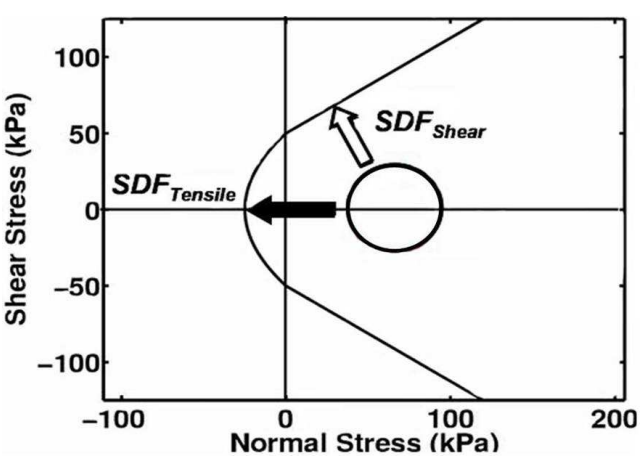

Figure 3. The Mohr circle and modified Griffith failure envelope. The dark arrow displays how far the circle is from failing in a tensile manner indicated by the Griffith portion of the envelope. The white arrow displays the distance the circle is to failing in a shear manner indicated by the Coulomb portion of the envelope.

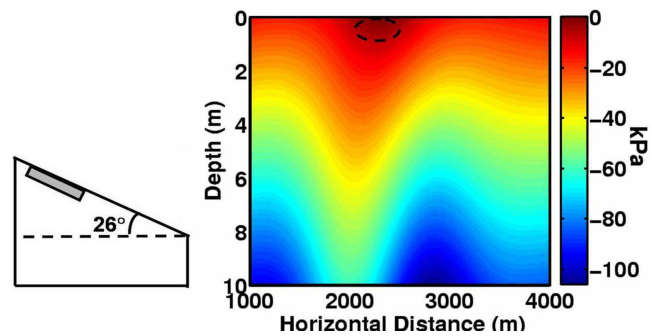

Figure 4. In the right panel, the stress difference to tensile failure is displayed for a slope of 26° and $c = 10$ kPa due to a P-wave with an incidence angle of 30°, normalized to a PGA= 0.1 g. The shaded area in the left panel indicates the region of the slope shown on the right. Failure occurs near the free surface, indicated by the circled region. Negative values of $SDF_{tensile}$ indicate the amount of stress necessary for tensile failure to occur.

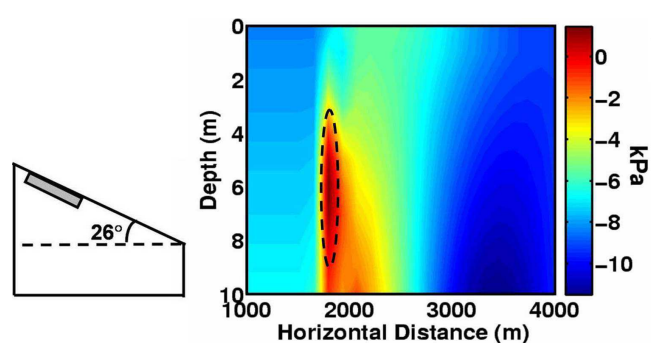

Figure 5. In the right panel, the stress difference to shear failure is displayed for a slope of 26° and $c = 10$ kPa due to a P-wave with an incidence angle of 30°, normalized to a PGA= 0.1 g. The shaded area in the left panel indicates the region of the slope shown on the right. Initiation of shear failure is located within the dotted lines.

failure. For larger shear stress, the envelope is defined by the Mohr-Coulomb equation. The region of the failure envelope first encountered by the Mohr circle determines the type of failure [*Bourne and Willemse*, 2001]. The stability of the slope is characterized by the distance of the Mohr circle to the failure envelope. As shown in Figure 3, we use the stress difference-to-failure (SDF) to quantify the proximity of any stress tensor to either shear or tensile failure. Failure takes place when either SDF_{shear} or $SDF_{tensile}$ is equal to zero, whichever occurs first [*Bourne and Willemse*, 2001]. A stable stress state is represented as negative values of SDF.

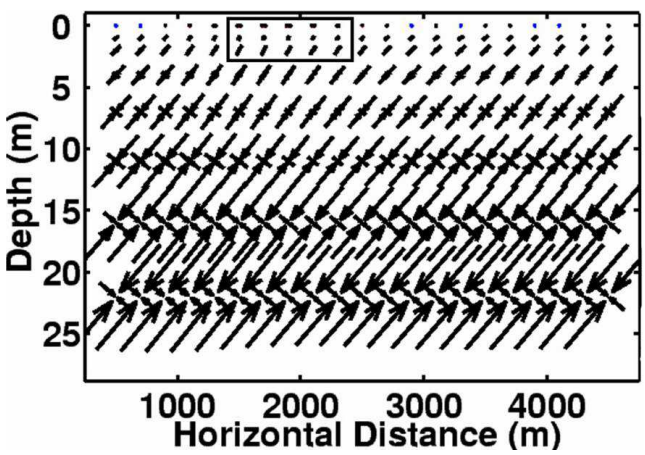

Figure 6. Principal stress components and directions computed for the 26° slope due to a P-wave with an incidence angle of 30°, normalized to a PGA= 0.1 g. Inward arrows represent compressional stress, while outward pointing arrows indicate extensional stress, noticeable at the near surface where tensile failure is found. The box is enlarged in Figure 7.

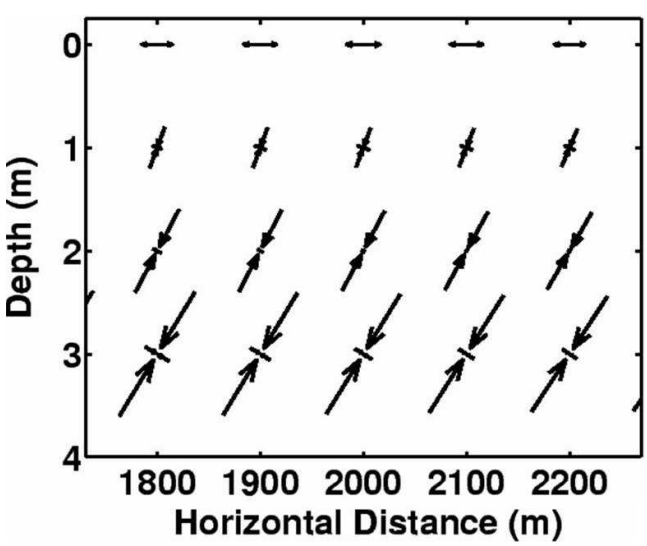

Figure 7. Principal stresses for a segment of the 26° slope. This shows that tensile stress exists to a depth of 1 m. At 2 m depth, compressional stress is dominant and the slope is prone to shear failure.

The equations to calculate SDF for the modified Griffith envelope are given as by [*Bourne and Willemse*, 2001]

$$SDF_{shear} = \left(\frac{\sigma_1 - \sigma_3}{2}\right) - \left(\frac{\sigma_1 + \sigma_3}{2}\right)\sin(\phi) - c\cos(\phi)\ , \tag{10}$$

$$SDF_{tensile} = \left(\frac{\sigma_1 - \sigma_3}{2}\right) - \left(\frac{\sigma_1 + \sigma_3}{2}\right) - \frac{1}{2}c\ . \tag{11}$$

3.1. Homogeneous Infinite Slope

We use this stress model to analyze triggered failure in an unsaturated, 26° slope which has a constant density of 2,000 kg/m^3, $c = 10$ kPa, and $\phi = 32°$. Before dynamic stress disrupts the slope, failure of the static slope takes place at 37°. When a slope is cohesive, such as in this example, static failure can occur at a slope angle larger than the internal angle of friction.

Even though an S-wave generates larger stress at the surface, a P-wave normalized to the same PGA produces the same failure mechanisms as does the S-wave. Figure 4 shows the stress difference to tensile failure in this slope due to a P-wave with an angle of incidence of 30°, normalized to a PGA of 0.1 g.

For a given instant in time, dynamic stress is great enough to produce tensile failure shown as the circled region in dark red near the surface of the slope. The colorbar also indicates other locations within the slope that have not failed, or negative values of $SDF_{tensile}$. Shear failure, as shown in Figure 5, takes place at greater depth than tensile failure. There is a limited depth interval for shear failure where the approximate location failing in shear is circled.

The mechanism for failure can be explained by analyzing the principal stress components and directions calculated after dynamic stress is added to the static stress. Figure 6 shows the principal stresses for the 26° slope due to the incident P-wave. The direction of the arrows indicate principal stress direction while the length represents the magnitude of the principal stress component. Inward pointing arrows represent compressional stress. Outward pointing arrows near

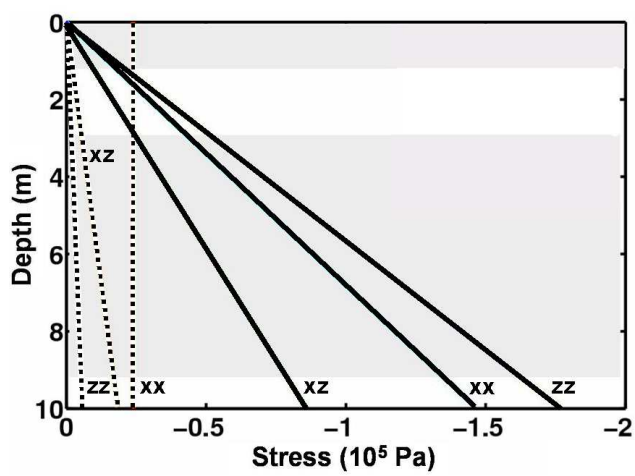

Figure 8. Stress components as a function of depth for the example outlined in Figures 4-5, at a horizontal distance of 2,000 m. Tensile failure for this 26° slope is outlined by the upper shaded region, while shear failure takes place in lower shaded region. The dotted lines represent the components of σ^{dyneq}, produced by equations (12)-(14), which are used in place of $\sigma^{dynamic}$ with depth. The solid lines represent the components of σ^{static}.

the surface indicate tensile stress, that which causes tensile failure as shown in Figure 4. The tensile stress near the surface is important, and the box in this image is enlarged for clarity in Figure 7.

Tensile stress is limited to the near-surface down to 1 m depth. The stresses at 2 m depth show a slight indication of extensional stress, but the dominant stress is compressive. At this depth, tensile failure does not occur. At 3 m, there is no tensile stress since both principal stress components are larger than zero. This further reduces the possibility for tensile failure to occur at this depth.

3.2. Dynamic Stress Near the Surface

To understand the depths of shear and tensile failure, we derive dynamic stress equations that express the stress in the near-surface in the acceleration at the free surface. These stress equations follow from Newton's Law and Hooke's Law. The significance of these equations is to determine the dynamic stress at depth when the PGA and direction of an incoming wave is known. The derivation of the equations for σ_{xx}^{dyneq}, σ_{zz}^{dyneq}, σ_{xz}^{dyneq} can be found in Appendix A:

$$\sigma_{xx}^{dyneq}(z) = \frac{4\mu(\lambda+\mu)}{\lambda+2\mu}\left(\frac{p}{2\pi f}\right)a_x \ , \tag{12}$$

$$\sigma_{zz}^{dyneq}(z) = -\rho a_z z \ , \tag{13}$$

$$\sigma_{xz}^{dyneq}(z) = -\left\{\rho a_x + \left(\frac{4\mu(\lambda+\mu)}{\lambda+2\mu}\right)\left(\frac{p}{2\pi f}\frac{\partial a_x}{\partial x}\right)\right\} z \ , \tag{14}$$

where p is the horizontal slowness of the incoming wave, f the peak frequency, a_x the acceleration in the horizontal direction, and a_z the acceleration in the vertical direction. Note that the tractions at the free surface vanish, producing the result shown in equation (6), while $\sigma_{xx}^{dyneq}(z=0)$ can be non-zero. *Gipprich* [2005] shows that these equations are a good approximation to the dynamic stress produced by the model by comparing how each stress component behaves with depth.

To investigate the depth of failure more closely, Figure 8 shows the static and dynamic stress components as a function of depth for the stress state of Figures 4-5 at a horizontal distance of 2,000 m. In this figure, we use the dynamic stress equations (12)-(14) in place of the dynamic stress with depth. The region of tensile failure is shaded at the near surface, and the region for shear failure is shaded at depth.

Figure 8 shows that all components of dynamic and static stress vanish at the free surface except one, σ_{xx}^{dyneq}. The three components of static stress depend on depth, as given in equations (2a)-(2c), and at the surface are equal to zero. Similarly, the two dynamic components σ_{xz}^{dyneq} and σ_{zz}^{dyneq} vanish at the surface due to the free-surface boundary condition. At the surface of this slope, tensile failure must be due to σ_{xx}^{dyneq}, since this is the only non-zero stress component. To further understand what determines the depth of tensile failure, we make the assumption that failure takes place when the tensile stress σ_{xx}^{dyneq} overcomes the compressive static stress σ_{zz}^{static}. We use σ_{zz}^{static} as a proxy of the compressive stress since this is the next largest stress near the surface, and it increases faster than any other stress component with depth. The tensile stress is larger than the compressive stress when

$$\left|\sigma_{xx}^{dyneq}\right| > \sigma_{zz}^{static} \ , \tag{15}$$

substituting the static stress equation (2b) for σ_{zz}^{static} gives

$$\left|\sigma_{xx}^{dyneq}\right| > \rho g z\cos(\theta) \ , \tag{16}$$

and solving for the depth of failure,

$$z < \frac{\sigma_{xx}^{dyneq}}{\rho g\cos(\theta)} \ . \tag{17}$$

At the point of failure, the tensile stress is equal to the tensile strength of the slope. Because σ_{xx}^{dyneq} is constant with depth, and the only source of stress causing tensile failure, its value is approximately equal to tensile strength, represented by $c/2$,

$$\sigma_{xx}^{dyneq} \approx \frac{c}{2} \ , \tag{18}$$

and substituting this into equation (17) gives:

$$z < \frac{c}{2\rho g\cos(\theta)} \ . \tag{19}$$

Therefore, the depth of tensile failure depends on the tensile strength of the slope, and varies with density and slope angle. For this example, c =10 kPa, $\rho = 2,000$ kg/m^3 and $\theta = 26^\circ$ and from (19) the region of tensile failure is $z < 0.3$ m.

This analysis gives an estimate of the maximum depth of tensile failure without having to analyze $SDF_{tensile}$. As σ_{xx}^{dyneq} is constant with depth, and static stress increases with depth, there is a point where tensile failure no longer occurs due to the growth of compressive, static stress. This is a depth where static stress is large enough so that σ_{xx}^{dyneq} does not make a notable impact for tensile stress in the x-direction.

As shown in Figure 8 when shear failure takes place, all static stress components are larger than dynamic stress. Shear failure occurs at a depth when the smallest static stress component σ_{xz}^{static}, is approximately equal to the largest dynamic stress, σ_{xx}^{dyneq}:

$$\sigma_{xx}^{dyneq} \approx \sigma_{xz}^{static} \ . \tag{20}$$

Substituting the static stress equation (2c) for σ_{xz}^{static} gives:

$$\sigma_{xx}^{dyneq} \approx \rho g z\sin(\theta) \ , \tag{21}$$

and solving for depth,

$$z \approx \frac{\sigma_{xx}^{dyneq}}{\rho g\sin(\theta)} \ . \tag{22}$$

The depth of failure can be found by substituting dynamic stress equation (12) for σ_{xx}^{dyneq},

$$z \approx \frac{\frac{4\mu(\lambda+\mu)}{\lambda+2\mu}\left(\frac{p}{2\pi f}\right)a_x}{\rho g\sin(\theta)} \ . \tag{23}$$

The input parameters for this example are $\lambda = 5.0\times10^8$ Pa, $\mu = 5.0\times10^9$ Pa, $p = 0.000289$ s/m, $f = 1.0$ Hz, and, $a_x = 0.3$ m/s^2. Given this information, $z \approx 3.0$ m for initial shear failure. Equation (23) demonstrates that the depth of shear failure depends on several factors that include the PGA, as well as the horizontal slowness.

This analysis relates the depths of shear and tensile failure in the slope to the dependence of dynamic stress with depth. Statically, the entire slope at 26° is stable, but when a plane wave is incident on the slope, in the near-surface, σ_{xx}^{dyneq} creates tensile failure in the x-direction. Deeper in the slope, σ_{xx}^{dyneq} is still the dominant dynamic stress component, but it is smaller than the static stress. When each component of σ^{total} is positive, tensile failure can no longer take place and when large enough, compressive stress causes

shear failure to occur. There is a depth below shear failure when failure no longer takes place. We see in equations (12)-(14) that dynamic stress is related to either the horizontal or vertical component of the PGA, while the static stress equations (12)-(14) are related to the gravitation acceleration. Because the PGA is normalized to a value less than the gravitational acceleration, at depth, the static stress components will become larger than the dynamic stress components. The graph in Figure 8 shows this relationship. At a depth where dynamic stress is small in comparison to the static stress, it has little influence on the total stress field and no longer triggers failure, which in this example, this takes place at a depth near 9 m.

3.3. Layered Slope

Following the description of a layered slope by *Terzaghi et al.* [1996], we focus on the failure analysis of an unsaturated slope with two layers parallel to the surface where the shallow upper meters represent a weathered layer overlying a stronger, sedimentary layer. Because weathering is largely confined to the upper meters of the slope, this produces a region of lower strength and, thus, an area more prone to slope failure than the underlying sedimentary layer [*Selby*, 1993].

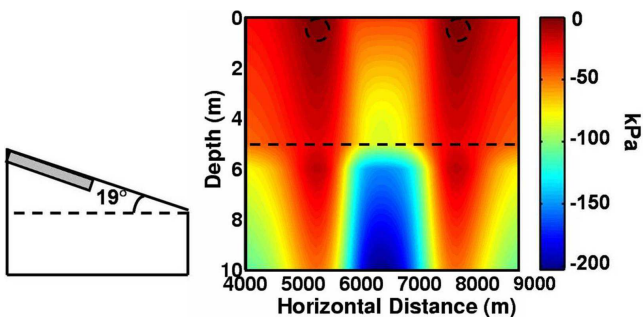

Figure 9. In the right panel, the stress difference to tensile failure is displayed for a layered slope of 19° and $c = 10$ kPa due to an S-wave with an incidence angle of 30°, normalized to a PGA= 0.1 g. The boundary between the two layers is indicated by the dotted line. The shaded area in the left panel indicates the region of the slope shown on the right. Failure occurs at the near surface, indicated by the circled regions.

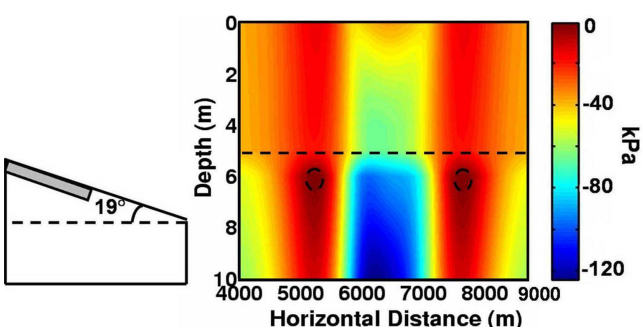

Figure 10. In the right panel, the stress difference to shear failure is displayed for a layered slope of 19° and $c = 50$ kPa due to an S-wave with an incidence angle of 30°, normalized to a PGA= 0.1 g. The boundary between the two layers is indicated by the dotted line. The shaded area in the left panel indicates the region of the slope shown on the right. The initiation of shear failure is circled at 6 m depth.

The low velocity layer, 5 meters deep, has parameters α_1, β_1, ρ_1, ϕ_1 and c_1 that are smaller than those for the sedimentary layer, α_2, β_2, ρ_2, ϕ_2 and c_2. The parameters used in the layered and homogeneous models are shown in Table 1. For the homogeneous case, parameters represent soil in a slope. This is the first step to understanding failure in a constant medium, without having to model fractures that occur in stronger material such as rock. The upper, weathered layer in the layered model represents weak, unconsolidated soil, and is characterized by parameters similar to those for the homogeneous model. We use the same values of cohesion and internal angle of friction for the homogeneous model and weathered layer, so we can see how failure compares in the upper meters of the slope, where tensile failure tends to occur.

The interface between the two layers represents a solid/solid boundary. Because of Snell's law, the horizontal slowness of the incident wave remains the same while crossing the interface between layers during the reflection/transmission process [*Aki and Richards*, 2002].

Overall, given the difference in dynamic stress and the parameters outlined in Table 1, the mechanisms of failure for a layered slope are the same as the homogeneous model. A layered slope produces tensile failure in the near surface and shear failure in both upper and lower layers at depth. For the layered example, we show failure due to an S-wave to demonstrate the failure mechanisms are the same for those produced with the P-wave. The stress difference to failure produced by an S-wave with an incidence angle of 30°, normalized to a PGA of 0.1 g is shown in Figures 9 and 10. Since the dynamic stress produced by an S-wave is larger than for a P-wave, failure takes place at shallower slopes than seen in the homogeneous case. Shear and tensile failure take place in the layered medium for a slope of 19°, while statically, failure for the entire slope occurs at 40°. These figures show that there are two distinct locations of failure, each providing a different mechanism of failure. The weathered layer is initially failing in a tensile manner near the surface up to 1 m depth, while the remainder of that layer does not fail. Below the interface, the only indication of failure is at 6 m depth, which is in shear.

The thickness of the upper layer (5 m) is a fraction of the wavelength of the incoming wave, which is 800 m for a frequency of 1.0 Hz. Because the wavelength is much larger

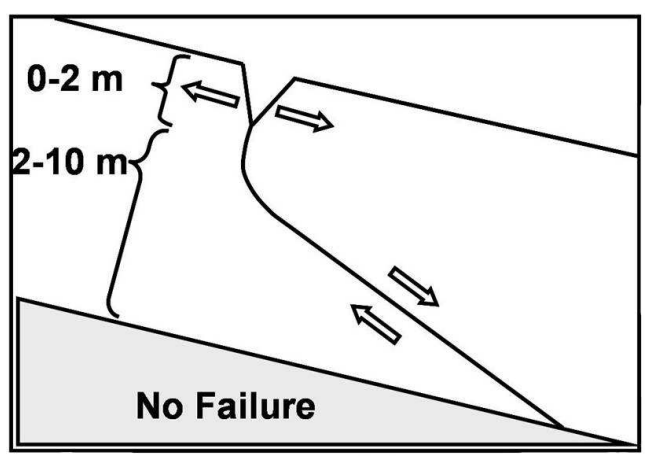

Figure 11. Combining the two mechanisms of failure indicated by the model and how they work together to create slope failure. Tensile failure occurs in the upper meters near the surface, while shear failure takes place at greater depth, below which, failure will not occur.

Table 1. Parameter values used in each slope model.

Model	α	β	ρ	ϕ	c
Homogeneous	1730 m/s	500 m/s	2000 kg/m^3	32°	10 kPa
Layered: Low Velocity	1500 m/s	800 m/s	1500 kg/m^3	32°	10 kPa
Layered: Sedimentary	2200 m/s	1000 m/s	2200 kg/m^3	40°	50 kPa

than the depth of this layer, the weathered layer has little impact on the dynamic stress. Therefore, for the same failure criteria, slope instability and failure in the layered slope ultimately resembles that of the homogeneous model. Because the layered slope contains physical properties that vary with depth, it is impossible to use the dynamic stress equations (12)-(14) as an approximation for the dynamic stress in the homogeneous slope.

This analysis shows that the presence of the weathering layer does not change the dynamic stress in the near-surface and failure occurs in the same manner as previously outlined.

4. Discussion

We describe the role of shear and tensile failure in the triggering of landslides. Our model provides evidence for the initiation of tensile failure in the near-surface and shear failure at depth in a slope subject to dynamic stress.

Figure 11 shows the depths indicated by the model for each type of failure. Due to dynamic stress, the upper meters of the slope tend to be in a state of extension, leading to tensile failure. At greater depths, shear failure takes place, while below this depth, failure no longer occurs. This figure shows that both failure mechanisms work together to cause landslides. Stress concentrations build as tensile (shear) failure initiates, inducing shear (tensile) failure. We are unable to determine from this model which type of failure occurs first in a slope, but this helps to link how the shear and tensile failure mechanisms produced from the model can actually occur in nature.

This project provides an additional viewpoint about the manner in which particular earthquakes cause slope failure. Given particular slope information we can test the susceptibility to both shear and tensile failure due to varying dynamic stress. Further, this work may help to improve methods which are currently in use. This could lead to changes in these methods by incorporating ways to measure tensile failure in addition to shear failure, as well as monitoring the dynamic stress produced from an earthquake. This project provides insight into the generation of slope failure and helps to create a more complete dynamic model.

Appendix A: Derivation of Dynamic Stress Equations

Given Newton's Law and Hooke's Law:

$$-\rho\omega^2 U_x = \frac{\partial \sigma_{xx}}{\partial x} + \frac{\partial \sigma_{xz}}{\partial z} , \tag{A1}$$

$$-\rho\omega^2 U_z = \frac{\partial \sigma_{xz}}{\partial x} + \frac{\partial \sigma_{zz}}{\partial z} , \tag{A2}$$

$$\sigma_{xx} = (\lambda + 2\mu)\frac{\partial U_x}{\partial x} + \lambda \frac{\partial U_z}{\partial z} , \tag{A3}$$

$$\sigma_{zz} = \lambda \frac{\partial U_x}{\partial x} + (\lambda + 2\mu)\frac{\partial U_z}{\partial z} , \tag{A4}$$

$$\sigma_{xz} = \mu \left(\frac{\partial U_z}{\partial x} + \frac{\partial U_x}{\partial z} \right) . \tag{A5}$$

At the surface, $\sigma_{zz}(z = 0) = \sigma_{xz}(z = 0) = 0$. We want to find how stress behaves near the free surface and express this in the displacement. Since the z-derivative of displacement cannot be measured, we eliminate $\partial U_z/\partial z$ from (A3)-(A4) by taking $(\lambda + 2\mu)\,(A3) - (\lambda)(A4)$:

$$(\lambda + 2\mu)\,\sigma_{xx} - \lambda\sigma_{zz} = \left((\lambda + 2\mu)^2 - \lambda^2\right) \frac{\partial U_x}{\partial x} . \tag{A6}$$

At the surface, $\sigma_{zz} = 0$, hence,

$$\sigma_{xx}^{(0)} = \frac{4\mu\,(\lambda + \mu)}{\lambda + 2\mu}\frac{\partial U_x}{\partial x} , \tag{A7}$$

where $\sigma_{ij}^{(0)}$ refers to the stress at the surface of the slope. Using a Taylor series expansion, $\sigma_{xx}(z) = \sigma_{xx}^{(0)} + O(z)$. The first term gives the dominant contribution of σ_{xx} near the surface, which is (A7) in this approximation. Since $\sigma_{zz}^{(0)} = 0$,

$$\sigma_{zz}(z) = \frac{\partial \sigma_{zz}^{(0)}}{\partial z} z + O(z^2) . \tag{A8}$$

$\partial \sigma_{zz}^{(0)}/\partial z$ is found by evaluating (A2) at $z = 0$, where σ_{xz} vanishes at the free surface, hence

$$-\rho\omega^2 U_z^{(0)} = \frac{\partial \sigma_{zz}^{(0)}}{\partial z} . \tag{A9}$$

Inserting this into (A8) gives:

$$\sigma_{zz}(z) = -\rho\omega^2 U_z^{(0)} z + O(z^2) . \tag{A10}$$

Similarly,

$$\sigma_{xz}(z) = \frac{\partial \sigma_{xz}^{(0)}}{\partial z} z + O(z^2) . \tag{A11}$$

Substitute (A7) into (A1) to evaluate this derivative at the free surface,

$$-\rho\omega^2 U_x = \left\{ \frac{\partial}{\partial x} \left(\frac{4\mu(\lambda + \mu)}{\lambda + 2\mu} \frac{\partial U_x}{\partial x} \right) \right\} + \frac{\partial \sigma_{xz}}{\partial z} , \tag{A12}$$

$$\frac{\partial \sigma_{xz}}{\partial z} = -\rho\omega^2 U_x - \left\{ \frac{\partial}{\partial x} \left(\frac{4\mu(\lambda + \mu)}{\lambda + 2\mu} \frac{\partial U_x}{\partial x} \right) \right\} . \tag{A13}$$

Therefore, the dynamic stress equations for the near-surface are:

$$\sigma_{xx}^{dyneq}(z) = \frac{4\mu(\lambda + \mu)}{\lambda + 2\mu} \frac{\partial U_x^{(0)}}{\partial x} + O(z) , \tag{A14}$$

$$\sigma_{zz}^{dyneq}(z) = -\rho\omega^2 U_z^{(0)} z + O(z^2) , \tag{A15}$$

$$\sigma_{xz}^{dyneq}(z) = -\left\{ \rho\omega^2 U_x^{(0)} + \frac{\partial}{\partial x} \left(\frac{4\mu(\lambda + \mu)}{\lambda + 2\mu} \frac{\partial U_x^{(0)}}{\partial x} \right) \right\} z + O(z^2) . \tag{A16}$$

For a plane wave, the displacement is given by:

$$U(x, z, t) = U(t - px, z) , \tag{A17}$$

where p is the slowness or ray parameter. Therefore, the derivative of displacement is expressed as:

$$\frac{\partial U_x}{\partial x} = -p\frac{\partial U_x}{\partial t} = -pv \ , \tag{A18}$$

where v is the particle velocity. In the frequency domain, this relationship can be written as:

$$\frac{\partial U_x}{\partial x} = \frac{-p}{-i\omega}a_x = \frac{p}{2\pi i f}a_x \ , \tag{A19}$$

where a_x is acceleration, and f the frequency of the wave. The derivative of displacement is approximately equal to:

$$\left|\frac{\partial U_x}{\partial x}\right| \approx \left|\frac{p}{2\pi f}a_x\right| \ . \tag{A20}$$

The slowness, p, is also related to the angle of incidence and the velocity at the surface,

$$p = \frac{sin(i_p)}{v_p} = \frac{sin(i_s)}{v_s} \ . \tag{A21}$$

By substituting (A20) for the derivative of displacement in equations (A14)-(A16), the stress components are related to slowness and, hence, the angle of incidence of a plane wave,

$$\sigma_{xx}^{dyneq}(z) = \frac{4\mu(\lambda+\mu)}{\lambda+2\mu}\left(\frac{p}{2\pi f}\right)a_x \ , \tag{A22}$$

$$\sigma_{zz}^{dyneq}(z) = -\rho a_z z \ , \tag{A23}$$

$$\sigma_{xz}^{dyneq}(z) = -\left\{\rho a_x + \left(\frac{4\mu(\lambda+\mu)}{\lambda+2\mu}\right)\left(\frac{p}{2\pi f}\frac{\partial a_x}{\partial x}\right)\right\}z \ . \tag{A24}$$

Acknowledgments. We would like to express appreciation to the National Earthquake Hazards Reduction Program (NEHRP) of the U. S. Geological Survey which has funded this research through award #04HQGR0108. Additionally, we extend our thanks to Dr. Matthew Haney for providing his finite-element code.

Notation

σ^{static} Static stress components, Pa;

$\sigma^{dynamic}$ Dynamic stress components produced by the model, Pa;

σ^{dyneq} Dynamic stress components produced by equations, Pa;

c Cohesion, Pa;

ϕ Internal angle of friction, degrees;

λ Lamé elastic constant, Pa;

μ Lamé elastic constant, Pa;

ρ Density, kg/m^3;

θ Slope angle, degrees;

p Horizontal slowness of a plane wave, s/m;

f Frequency of a plane wave, Hz;

a_x Horizontal component of acceleration for a plane wave, m/s^2;

a_z Vertical component of acceleration for a plane wave, m/s^2;

References

Aki, K., and P. G. Richards (2002), *Quantitative Seismology*, 2nd ed., University Science Books.

Bourne, S. J., and E. J. Willemse (2001), Elastic stress control on the pattern of tensile fracturing around a small fault network at Nash Point, UK, *Journal of Structural Geology*, *23*, 1753–1770.

Brace, W. F. (1960), An extension of the Griffith theory of fracture to rocks, *Journal of Geophysical Research*, *65*, 3477–3480.

Das, B. M. (1997), *Advanced Soil Mechanics*, 2nd ed., Taylor and Francis.

Frankel, A. D. (1999), Earthquake ground motion: How does the ground shake?, *Science*, *283*, 2032–2033.

Gipprich, T. L. (2005), The role of shear and tensile failure in dynamically triggered landslides, Master's thesis, Colorado School of Mines.

Haney, M. M. (2004), An investigation of sealing and episodic pulsing of fluids at a minibasin-bounding growth fault from seismic reflection images, Ph.D. thesis, Colorado School of Mines.

Jaeger, J. C., and N. G. Cook (1976), *Fundamentals of Rock Mechanics*, John Wiley and Sons, Inc.

Jibson, R. W. (1993), Predicting earthquake-induced landslide displacements using Newmark's sliding block analysis, *Transportation Research Record*, *1411*, 9–17.

Jibson, R. W., E. L. Harp, and J. A. Michael (2000), A method for producing digital probabilistic seismic landslide hazard maps, *Engineering Geology*, *58*, 271–289.

Mello, U. T., and L. F. Pratson (1999), Regional slope stability and slope-failure mechanics from the two-dimensional state of stress in an infinite slope, *Marine Geology*, *154*, 339–356.

Middleton, G. V., and P. R. Wilcock (1994), *Mechanics in the Earth and Environmental Sceinces*, Cambridge University Press.

Newmark, N. M. (1965), Effects of earthquakes on dams and embankments, *Geotechnique*, *15*, 139–160.

Savage, W. Z., and H. S. Swolfs (1992), Near-surface crustal stresses - theory and application, *Trends in Geophysical Research*, *1*, 217–250.

Selby, M. J. (1993), *Hillslope Materials and Processes*, 2nd ed., Oxford University Press.

Terzaghi, K., R. B. Peck, and G. Mesri (1996), *Soil Mechanics in Engineering Practice*, 3nd ed., John Wiley and Sons, Inc.

T. Gipprich, Center for Wave Phenomena and Department of Geophysics, Colorado School of Mines, 1500 Illinois Street, Golden, CO 80401, USA. (tgippric@mines.edu)

R. Snieder, Center for Wave Phenomena and Department of Geophysics, Colorado School of Mines, 1500 Illinois Street, Golden, CO 80401, USA. (rsnieder@mines.edu)

R. Jibson, The United States Geological Survey P. O. Box 25046, Mail Stop 966, Golden, CO 80225, USA. (jibson@usgs.gov)

W. Kimman, Center for Wave Phenomena and Department of Geophysics, Colorado School of Mines, 1500 Illinois Street, Golden, CO 80401, USA. (wkimman@mines.edu)